Excitation mechanisms in moderate-energy Na^+-Ar collisions

S. Kita,[1] T. Hasegawa,[2,*] H. Tanuma,[2,†] and N. Shimakura[3]
[1]*Department of Physics, Nagoya Institute of Technology, Gokiso, Showa-ku, Nagoya 466, Japan*
[2]*Research Institute for Scientific Measurements, Tohoku University, Katahira, Aoba-ku, Sendai 980, Japan*
[3]*Department of Chemistry, Faculty of Science, Niigata University, Ikarashi, Niigata 950-21, Japan*
(Received 12 December 1994)

By means of differential energy-transfer measurements, excitation mechanisms in Na^+-Ar collisions have been studied at laboratory collision energies of $50 \le E_{lab} \le 1500$ eV. In these experiments, doubly differential cross sections have been measured over nearly the whole angular range in the center-of-mass system by simultaneously detecting both scattered and recoiled particles (Na^+, Na, Ar^+, and Ar) at laboratory angles of $2° \le \theta \le 92°$. The Na^+ ions and Na atoms scattered inelastically were observed at reduced angles of $\tau > 3.5$ keV deg and collision energies of $E_{lab} > 500$ eV. For energies of $500 < E_{lab} < 1000$ eV, the dominant inelastic signal is due to one-electron charge transfer, while for $E_{lab} > 1000$ eV, two-electron excitation as well as one-electron excitation were observed. The electronic transitions in the Na^+-Ar collisions are classified into two types of excitation mechanisms. One type is the one-electron transition that takes place at internuclear distances of $R < R_{C1} = 1.07$ Å. The other type is the one- and two-electron transitions that occur at distances of $R < R_{C2} = 0.45$ Å. These critical distances $R_C = 1.07$ and 0.45 Å are close to $|r_i \pm r_j| = 0.96$ and 0.38 Å, respectively, evaluated from the ionic and atomic radii.

PACS number(s): 34.50.Fa, 34.20.Cf

I. INTRODUCTION

In moderate-energy collisions of closed-shell particles, electronic transitions depend strongly on colliding systems [1–14]. For symmetric and quasisymmetric systems, excitation probability is especially high even at lower collision energies [1–8], while the probability for asymmetric systems is low [9–13], except for Li^+-Ne [11] and He-rare gas systems [14]. Another remarkable feature in the inelastic collisions of closed-shell particles is the fact that excitation into a doubly excited state lying at a higher energy is observed with a high probability and with the threshold energy being almost the same as that for one-electron excitation. Excitation in low-energy collisions takes place through the curve crossing between the ground-state and excited-state potentials V_1 and V_2. The excitation is characterized by crossing radius R_C, interaction energy $V_{12}(R_C)$, and the difference in slopes of the two potentials $\Delta S(R_C)$ at the crossing [15]. The excitation processes are qualitatively interpreted by an electron promotion model [16]. In order to discuss quantitatively the excitation mechanisms, one has to evaluate the crossing parameters by collision experiments or *ab initio* calculations. Unfortunately, the accuracy of the calculation is still not sufficient for many-electron systems.

Repulsive potentials between closed-shell particles have been extensively determined in the range $0.1 < V(R) < 10$ eV, by measuring integral cross sections as a function of collision energy [17–20]. The potentials evaluated both experimentally and theoretically have a simple character [21] and were found to be related to the overlap of electron clouds of colliding partners [20,22]. Very similar discussions on the repulsive potentials have also been reported in the study of atomic interactions with solid surfaces [23]. The radius R_C, which characterizes the potential crossing, also has a close relation to the atomic radii of colliding partners [24–26]. This suggests that the electron-density distributions ρ_i and ρ_j of the colliding partners i and j govern the potential curve crossing.

In earlier papers, we have reported differential scattering experiments on excitation and autoionization in the quasisymmetric Na^+-Ne and K^+-Ar systems at lower collision energies [8]. In this study, differential scattering in an asymmetric Na^+-Ar system has been investigated over a wide range of laboratory angles of $2° < \theta < 92°$ and at moderate laboratory energies of $50 \le E_{lab} \le 1500$ eV. The velocity of scattered particles was analyzed by a time-of-flight (TOF) technique. For the Na^+-Ar collisions, an energy-loss spectrum of the Na^+ ions scattered at $E_{lab} = 5$ keV and $\theta = 4.5°$ [10], and an energy spectrum of electrons ejected from autoionizing states of Ar atoms at $E_{lab} = 15$ keV [27] have been briefly reported, but, to our knowledge, no investigation on the excitation mechanisms in moderate-energy collisions has been reported up to now.

Differential scattering of Li^+ ions from rare gases has already been studied at energies of $E_{lab} > 500$ eV and the smaller angles $\theta < 30°$, and the excitation mechanisms have been discussed in detail [11]. In order to compare with the results of Na^+-Ar, differential scattering in the Li^+-Ar collisions has also been studied at $70 \le E_{lab} \le 350$

*Present address: Research and Development Division, Asahi Glass Co., Ltd., 3-474-2 Tsukagoshi, Saiwai-ku, Kawasaki 210, Japan.
†Present address: Department of Physics, Tokyo Metropolitan University, 1-1 Minami-ohsawa, Hachioji, Tokyo 192-03, Japan.

eV in this work.

Alkali-atom-rare–gas-atom systems contain an isolated electron outside two closed-shell cores, and are often referred to as quasi-one-electron systems. The transition of the isolated electron in low-energy collisions is considered to proceed through level crossing of the closed-shell cores. For Na-Ar collisions, the impact-parameter dependence of the Na($3s \rightarrow 3p$) transition has been studied at moderate collision energies by means of photon-particle coincidence measurements [28]. This transition has been related to the promotion of the outermost $3p$ electron of the Ar atom into higher empty ones, which corresponds to the direct excitation of Ar atoms in the Na^+-Ar collisions. We can, therefore, discuss directly the transition mechanism for Na-Ar by studying interactions of Na^+ ions with Ar atoms. The crossing radius for the Na($3s \rightarrow 3p$) transition is evaluated to be 2 a.u. (1.06 Å). Similar photon-particle coincidence measurements have also been performed for the transition $K(4s \rightarrow 4p)$ in low-energy K-Hg collisions [29], but the excitation mechanism is not clear at the present time.

II. EXPERIMENTS

A. Apparatus

Differential scattering experiments have been performed with a crossed-beam apparatus. Since the details of the apparatus have been given elsewhere [30] (and a schematic drawing of the apparatus is presented in Fig. 1 in Ref. [26]), only brief descriptions will be given here. The apparatus consists of five chambers: a main chamber, an ion source, a nozzle source followed by a collimation chamber, and a detector chamber.

The two beams cross each other perpendicularly in the main chamber, and particles scattered in-plane are detected by a rotatable secondary-electron multiplier (Hamamatsu R595). The primary Na^+ ions are produced by means of thermionic emission from the natural $(Na_2O)(Al_2O_3)(2SiO_2)$ on a heated platinum wire, and the $^6Li^+$ ions are obtained from the isotope-enriched $(^6Li_2O)(Al_2O_3)(2SiO_2)$ [31]. The ions are accelerated to the desired energies of $50 \leq E_{lab} \leq 1500$ eV in a lens system, and are collimated by two slits into an angular spread of approximately 0.25° full width at half maximum (FWHM). The secondary Ar beam is injected into the collision chamber as a supersonic beam [32]. At the stagnation pressure of $P_0 = 1200$ Torr in the nozzle beam source, the flow velocity and angular spread of the beam are $u = 560$ m/s and $\Delta\theta = 1.4°$ FWHM, respectively.

For time-of-flight measurements the ion beam is pulsed with a pair of condenser plates in front of collimating slits [33]. The flight-path length from the scattering center to the detector is approximately 50 cm. Overall angular resolution for the scattered particles is approximately 0.35° FWHM. Time resolution $\Delta t/t$ in the TOF measurements is 1/700 for an ion energy $E_{lab} = 1500$ eV at a scattering angle $\theta = 5°$. The laboratory angle θ is determined with respect to the primary ion-beam axis with an accuracy of 0.05°.

In this apparatus, both ions and neutral atoms scattered into an angle θ are detected simultaneously. By sweeping off the scattered ions with a positive high voltage, only the neutral particles can be detected through the multiplier. The ions are accelerated by a negative high voltage ($V_{EM} = -2700$ V), which is applied to the first dynode of the multiplier, and impinge on the multiplier with high velocity. The detection efficiency ε for the ions can therefore be estimated to be unity. However, the efficiency ε for the neutral atoms, which hit the first dynode with lower velocity, is smaller than unity if the impinging energy is lower than a critical energy. Since both ions and atoms that belong to same reaction channel, Na^+-Ar and Na-Ar^+, are detected simultaneously in the measurements, we could evaluate the detection efficiency ε of the recoiled Ar atoms at impinging energies of $50 < E_{im} < 1100$ eV and of the Na atoms produced by charge transfer at energies of $300 < E_{im} < 1100$ eV. For this evaluation of the efficiency ε, we have used the relation $\sigma_s(\theta_s)d\omega_s = \sigma_r(\theta_r)d\omega_r$ between differential cross section (DCS) $\sigma_s(\theta_s)$ of particles scattered into a laboratory angle of θ_s and DCS $\sigma_r(\theta_r)$ of those recoiled into an angle θ_r, where the angles θ_s and θ_r belong to an identical center-of-mass (c.m.) angle Θ and $d\omega$'s are elements of the solid angle [34]. The efficiency ε's for the Ar atoms and the Na atoms are almost the same within the experimental uncertainty ±15%. According to the experimental results, the efficiency ε is unity at $E_{im} > 1000$ eV, and decreases gradually with decreasing energy at $350 < E_{im} < 1000$ eV. For $E_{im} < 350$ eV, ε decreases steeply with decreasing energy.

By detecting scattered and recoiled particles with the calibrated multiplier, differential cross sections over nearly the whole angular range in the c.m. system have been determined in this study.

B. Time-of-flight spectra

1. Na^+-Ar collisions

Figure 1 shows the TOF spectra of the particles scattered into the angle $\theta = 18°$ in the Na^+-Ar collisions at $E_{lab} = 1000$ eV. The abscissa is the flight time in units of μs and the ordinate is the relative intensity. In the figure the most intensive peak A_0 is normalized to unity. Figure 1(a) exhibits the spectrum of scattered ions and neutral atoms, while Fig. 1(b) is the spectrum of neutral atoms measured by rejecting the ions with a positive high voltage. In the figure, peaks A_0 and C_1 are attributed to ions, while peaks B_1, D_0, and D_1 are due to neutral atoms.

The intense peak A_0 is ascribed to the Na^+ ions scattered elastically, while the dominant neutral peak D_0 is due to the Ar atoms recoiled elastically from the Na^+ ions. Two peaks B_1 and C_1 are ascribed to the Na atoms and Ar^+ ions, respectively, produced by the charge-exchange reaction

$$Na^+ + Ar \rightarrow Na(3s) + Ar^+ - 10.6 \text{ eV} . \quad (1)$$

Flight-time locations of the Na atoms and Ar^+ ions produced by reaction (1) are indicated by the arrows 1 and 2

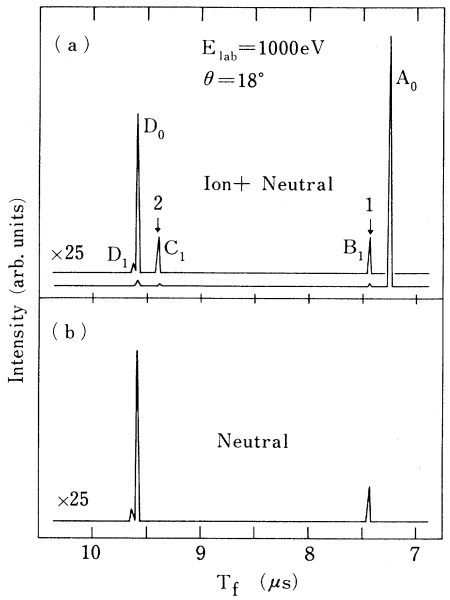

FIG. 1. Typical TOF spectra in the Na^+-Ar collisions measured at $E_{lab}=1000$ eV and $\theta=18°$. (a) Spectrum of ions and neutral atoms, and (b) only for neutral atoms. Peaks A_0 and B_1 are due to Na^+ ions and Na atoms, respectively. Peak C_1 is attributed to Ar^+ ions. Peaks D_0 and D_1 are due to Ar atoms. Arrows 1 and 2 are TOF locations of the Na atoms and Ar^+ ions, respectively, produced by reaction (1). Peaks B_1, C_1, D_0, and D_1 are magnified by a factor of 25.

in Fig. 1 (a), respectively. The weak neutral signal D_1 is due to the Ar atoms recoiled inelastically by the reaction

$$Na^+ + Ar \rightarrow Na^+ + Ar(4s) - 11.6 \text{ eV} . \quad (2)$$

It must be noticed that the Ar atoms and Ar^+ ions recoiled into a small angle θ belong to backward scattering, c.m. angle $\Theta \simeq 144°$ for $\theta=18°$, because the angle θ is determined here with respect to the beam axis of the primary Na^+ ions. The intensity of the Ar signal D_1 in Fig. 1 is approximately 30% of that of the Ar^+ signal C_1. Thus, the inelastic signal observed at $E_{lab}=650$ eV is predominantly due to reaction (1), which is the electronic transition into the first excited state.

Except for small angles of $E_{lab}\theta<5$ keV deg and large angles of $\theta>80°$, all the TOF spectra measured at $E_{lab}>500$ eV have four types of signals, i.e., Na^+ ions (peak A), Na atoms (B), Ar^+ ions (C), and Ar atoms (D). However, at lower energies of $E_{lab}<500$ eV, the spectra are composed of two elastic peaks A_0 and D_0.

Figure 2 exhibits energy-transfer spectra observed at $E_{lab}=1500$ eV and $\theta=27.5°$, where the abscissa is the energy transfer Q from kinetic to excitation energy of the colliding particles in units of eV. These spectra are deduced from a TOF spectrum by taking into account the Jacobian factor dQ/dt, where t means flight time. Figures 2(a) and 2(b) are the spectra of the Na^+ ions and the Na atoms, respectively. Figures 2(c) and 2(d) are of the Ar^+ ions and the Ar atoms, respectively. In Fig. 2(a) for Na^+ ions, a weak inelastic signal A_1 is observed around $Q=12$ eV as a shoulder of the elastic peak A_0. The signal A_1 is ascribed to the excitation of Ar atoms by reactions (2) and/or

$$Na^+ + Ar \rightarrow Na^+ + Ar(4p) - 12.9 \text{ eV} . \quad (3)$$

Peak B_1 of the Na atoms in Fig. 2(b) is also located around $Q=12$ eV. Peak B_1 has an energy width somewhat broader than that for elastic peak A_0 and is attributed to reactions (1) and

$$Na^+ + Ar \rightarrow Na(3p) + Ar^+ - 12.7 \text{ eV} . \quad (4)$$

Peaks C_1 and C_2 of the Ar^+ ions in Fig. 2(c) are located around $Q=11$ and 29 eV, respectively. Peak C_1 is due to charge-exchange reactions (1) and (4), the same as for peak B_1 in Fig. 2(b). Peak C_2 will mainly be attributed to the two-electron processes of the charge exchange with the target excitation

$$Na^+ + Ar \rightarrow Na(3s) + Ar^+[3p^4(^1D)4s] - 29.1 \text{ eV} , \quad (5)$$

and of the direct excitation of Ar atoms into an autoionizing state [27]

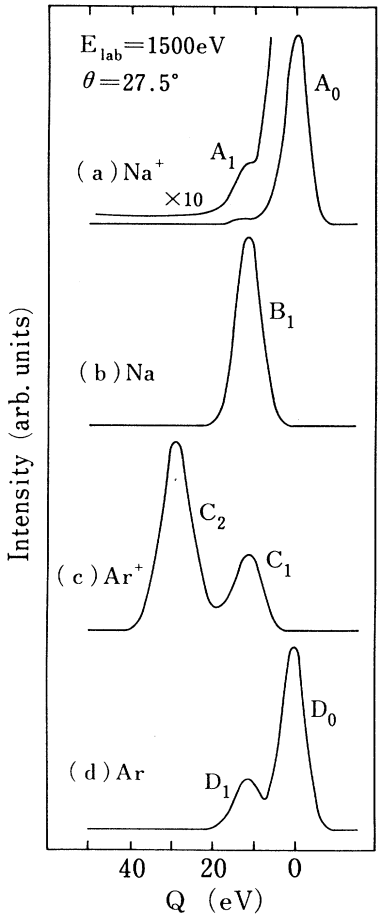

FIG. 2. Energy transfer spectra in the Na^+-Ar collisions measured at $E_{lab}=1500$ eV and $\theta=27.5°$. (a) Spectrum of Na^+ ions, (b) for Na atoms, (c) for Ar^+ ions, and (d) for Ar atoms. Peaks A_0 and D_0 correspond to elastic scattering. Peaks A_1, B_1, C_1, and D_1 are attributed to one-electron excitations, and peak C_2 is due to two-electron excitations.

$$Na^+ + Ar \rightarrow Na^+ + Ar[3p^4(^1D)4s^2] - 28.7 \text{ eV}$$
$$\downarrow$$
$$Ar^+ + e^- \quad . \tag{6}$$

There are several other exit channels with excitation energies close to those for reactions (5) and (6). The ejected electron spectrum measured at $E_{lab}=15$ keV [27], however, indicates that the main exit channel for autoionization is due to reaction (6). The main channel for the charge exchange of the two-electron process is then considered to be reaction (5), which has almost the same excitation energy as for reaction (6). Prominent Ar peak D_0 in Fig. 2(d) is the elastic signal, while peak D_1 located around $Q=11$ eV is ascribed to the excitation of Ar atoms by reactions (2) and (3).

Figure 3 shows energy transfer spectra of the Na^+ ions and Na atoms scattered into the large angle $\theta=75°$ at $E_{lab}=1500$ eV. Both Na^+ peak A_2 and Na peak B_2, which could not be observed at small angles, are located around $Q=29$ eV. The peak location $Q=29$ eV is the same as that for Ar^+ peak C_2 in Fig. 2(c). Peaks A_2 and B_2 are then attributed to reaction (6) of the two-electron excitation of Ar atoms and to the charge-exchange reaction (5) with target excitation, respectively. Thus, peaks A_2 and B_2 were observed only at large angles of θ, while the Ar^+ peak C_2 was at small angles of θ.

2. Li^+-Ar collisions

Figure 4 shows a typical TOF spectrum of the Li^+ ions and Li atoms scattered into the angle $\theta=34°$ at $E_{lab}=350$ eV. Peaks A_0 and A_1 are due to the Li^+ ions, while peak B_1 is ascribed to the Li atoms produced by the charge-exchange reaction. The peaks of Ar^+ ions and Ar atoms were also observed at large flight times, $T_f=22$–23 μs, but are not shown here. The scales Q_A and Q_B in the figure give energy transfers for Li^+ and Li, respectively. The intense Li^+ peak A_0 is due to the elastic scattering. Peak A_1 is located around $Q=12$ eV, and is attributed to the direct excitation of Ar atoms by the reactions

$$Li^+ + Ar \rightarrow \begin{cases} Li^+ + Ar(4s) - 11.6 \text{ eV} \\ Li^+ + Ar(4p) - 12.9 \text{ eV} \end{cases} . \tag{7}$$

Peak B_1 of the Li atoms located around $Q=11$ eV is attributed to the charge-exchange reaction

$$Li^+ + Ar \rightarrow Li(2s) + Ar^+ - 10.4 \text{ eV} \quad . \tag{8}$$

The peak locations of signals A_1 and B_1 depend somewhat on the angle. At large angles of $\theta > 40°$, the Li^+ peak A_1 is located around $Q=12.5$ eV, which indicates the dominance of the Ar($4p$) excitation. As will be mentioned below, the charge-exchange DCS $\sigma(\theta)_{B1}$ of signal B_1 has an oscillatory structure (see Fig. 10). Peak B_1 observed at the maxima of the DCS $\sigma(\theta)_{B1}$ is always located around $Q=11$ eV and is due to reaction (8). However, peak B_1 at the minima of the DCS is located around $Q=12.5$ eV and is attributed to the reaction

$$Li^+ + Ar \rightarrow Li(2p) + Ar^+ - 12.2 \text{ eV} \quad . \tag{9}$$

Thus, all the excitation signals observed in this study correspond to the one-electron transitions.

C. Differential cross sections

1. Na^+-Ar collisions

Measurements of differential cross sections (DCS's) have been performed at laboratory angles of $2° \leq \theta \leq 92°$ and collision energies of $50 \leq E_{lab} \leq 1500$ eV.

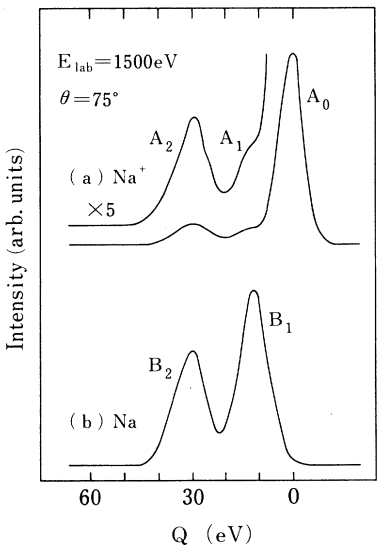

FIG. 3. Energy transfer spectra in the Na^+-Ar collisions measured at $E_{lab}=1500$ eV and $\theta=75°$. (a) Spectrum of Na^+ ions, and (b) for Na atoms. Peak A_0 corresponds to elastic scattering. Peaks A_1 and B_1 are due to one-electron excitations, and peaks A_2 and B_2 are attributed to two-electron excitations.

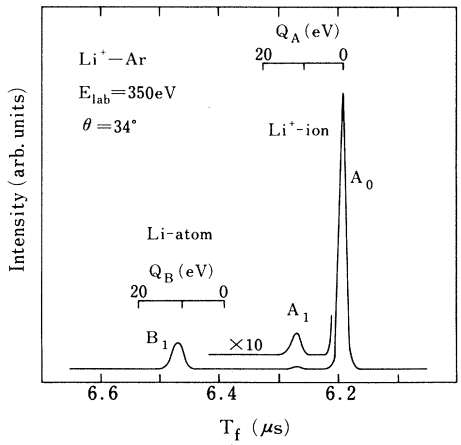

FIG. 4. Typical TOF spectrum in the Li^+-Ar collisions measured at $E_{lab}=350$ eV and $\theta=34°$. Peaks A_0 and A_1 are due to Li^+ ions, and peak B_1 is attributed to Li atoms. The scales Q_A and Q_B denote energy transfers for Li^+ ions and Li atoms, respectively. Peak A_1 is magnified by a factor of 10.

(i) *Elastic scattering.* As discussed above, the particles detected at energies of $E_{lab} < 500$ eV are the Na^+ ions and Ar atoms scattered elastically. Shown in Fig. 5 is the elastic DCS $\sigma(\Theta)\sin\Theta$ in the c.m. frame, which was deduced from the DCS $\sigma(\theta)$ in the laboratory system measured at $70 \leq E_{lab} \leq 350$ eV by taking into account the Jacobian factor for transformation [34]. The open circles are the DCS's deduced from the Na^+-ion data measured at $\theta < 92°$, while the solid circles for $E_{lab} = 200$ and 350 eV at large angles are the DCS's evaluated from the intensity of the Ar atoms at $\theta < 27°$ with the detection efficiency ε of the multiplier. The DCS's measured in this study are relative ones. The absolute values of the DCS's for $E_{lab} = 200$ and 350 eV were determined by using the experimental integral cross sections and the repulsive potential deduced experimentally at distances of $1.63 \leq R \leq 2.10$ Å [19],

$$V(R) = 11\,340 \exp(-4.68R) \text{ eV} . \quad (10)$$

The integral cross sections measured at $E_{lab} = 200$ and 350 eV are 16.78 and 14.93 Å^2, respectively [19,35]. The normalized results of the DCS are displayed in Fig. 5. The experimental DCS's at $\Theta < 10°$ for $E_{lab} = 200$ and 350 eV agree to within 10% with the DCS's calculated by employing Eq. (10), but at angles of $\Theta > 10°$ the agreement between the experiments and the calculations is not so good. This suggests that the potential of Eq. (10) is not accurate at smaller distances.

(ii) *Inelastic scattering.* Figure 6 exhibits the DCS's in the laboratory system measured at $E_{lab} = 650$ eV. The solid circles represent the DCS $\sigma(\theta)_{B1}$ of the Na atoms

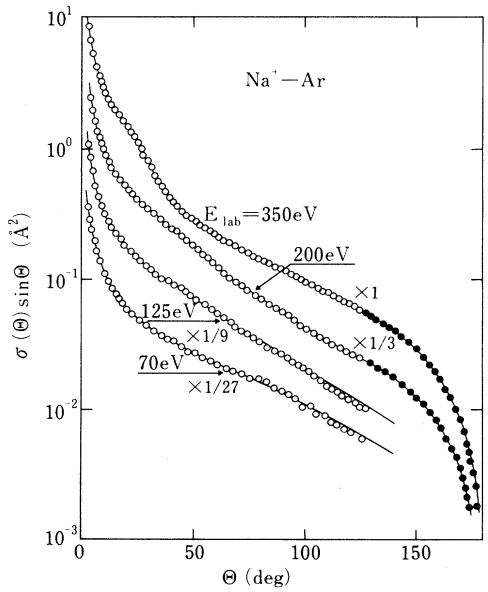

FIG. 5. Elastic DCS $\sigma(\Theta)\sin\Theta$ in the c.m. system for Na^+-Ar at $70 \leq E_{lab} \leq 350$ eV. ○ and ●, experimental DCS's evaluated from the intensity of the Na^+ ions and the Ar atoms, respectively. ——, the DCS calculated with the potential of Eq. (12). The DCS's for energies of $E_{lab} = 70$, 125, and 200 eV are shifted by the factors of $\frac{1}{27}$, $\frac{1}{9}$, and $\frac{1}{3}$, respectively.

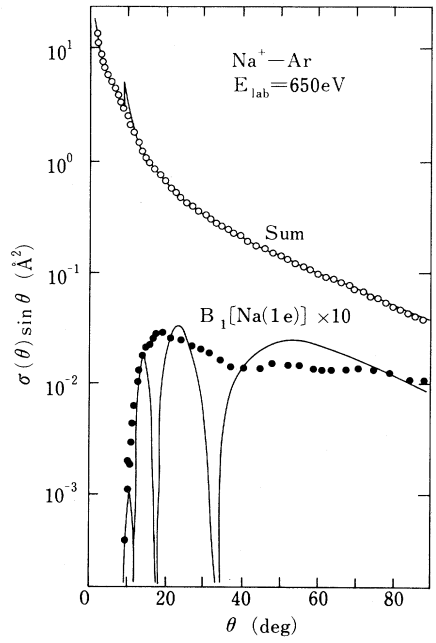

FIG. 6. Angular dependence of the DCS $\sigma(\theta)\sin\theta$ in the laboratory system for Na^+-Ar at energies of $E_{lab} = 650$ eV. ○, sum of the experimental DCS's of the scattered Na^+ ions and Na atoms. ●, experimental DCS of the Na atoms produced by a one-electron ($1e$) charge transfer multiplied by a factor of 10. ——, calculated DCS's.

produced by charge-exchange reaction (1) of the one-electron process, which was evaluated with the detection efficiency ε. The DCS $\sigma(\theta)_{A1}$ of the Na^+ ions for direct excitation of Ar atoms, reaction (2), could be only roughly evaluated to be less than 25% of the DCS $\sigma(\theta)_{B1}$ at $E_{lab} = 650$ eV. The open circles give the sum of the DCS's of Na^+ ions and Na atoms. The DCS's of Ar^+ ions and Ar atoms are not shown in the figure for clarity. The DCS $\sigma(\theta)_{B1}$ shows sharp onset around $\theta = 10°$ and has a weakly undulating structure at $\theta > 20°$.

Figure 7 shows the DCS's in the laboratory system of the Na^+ ions and Na atoms scattered from Ar atoms at $E_{lab} = 1500$ eV. The open and solid circles represent the summed DCS $\sigma(\theta)_{sum}$ and the elastic DCS $\sigma(\theta)_{A0}$, respectively. The open and solid triangles are the DCS's $\sigma(\theta)_{B1}$ and $\sigma(\theta)_{A1}$, respectively, of one-electron transitions. The open and solid squares are $\sigma(\theta)_{B2}$ for the charge transfer of the two-electron process and $\sigma(\theta)_{A2}$ for the two-electron excitation of Ar atoms into the autoionizing state, respectively. The intensity of the Na^+-ion signal A_1, $\sigma(\theta)_{A1}$, could be evaluated separately from the intensive elastic signal A_0 only at a limited angular range of $\theta \geq 10°$.

As is seen in Fig. 7, the DCS $\sigma(\theta)_{B1}$ begins to appear around $\theta = 2.5°$ and has a maximum around $\theta = 5°$. At the lower energies $E_{lab} \leq 1000$ eV, the direct excitation DCS $\sigma(\theta)_{A1}$ is less than 30% of the charge-transfer DCS $\sigma(\theta)_{B1}$. In the high-energy collisions at $E_{lab} = 1500$ eV, however, the DCS $\sigma(\theta)_{A1}$ at $\theta > 10°$ has (roughly say) al-

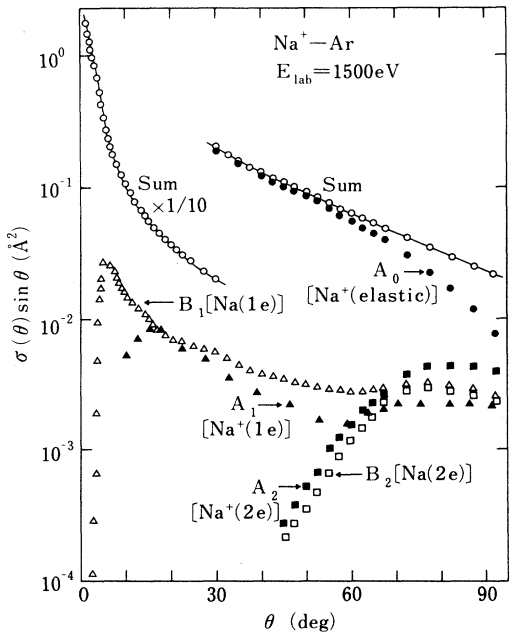

FIG. 7. Angular dependence of the DCS $\sigma(\theta)\sin\theta$ of the scattered Na^+ ions and Na atoms in the laboratory system for Na^+-Ar at $E_{lab}=1500$ eV. ○ and ●, experimental summed DCS $\sigma(\theta)_{sum}$ and elastic DCS $\sigma(\theta)_{A0}$, respectively. △ and ▲, experimental DCS's $\sigma(\theta)_{B1}$ and $\sigma(\theta)_{A1}$, respectively, of one-electron ($1e$) excitations. □ and ■, experimental DCS's $\sigma(\theta)_{B2}$ and $\sigma(\theta)_{A2}$, respectively, of two-electron ($2e$) excitations. ——, calculation of the elastic DCS. The summed DCS at $\theta<30°$ is shifted by a factor of $\frac{1}{10}$.

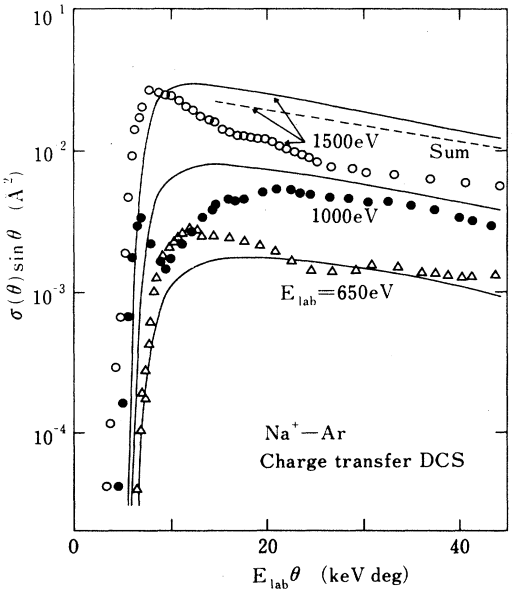

FIG. 8. Angular and energy dependences of the DCS $\sigma(\theta)_{B1}\sin\theta$ of one-electron charge transfer in the laboratory system for Na^+-Ar. △, ●, and ○, DCS's measured at $E_{lab}=650$, 1000, and 1500 eV, respectively. — — —, sum of the experimental inelastic DCS's, $\sigma(\theta)_{1e}=\sigma(\theta)_{A1}+\sigma(\theta)_{B1}$, for $E_{lab}=1500$ eV. ——, calculated DCS.

most the same magnitude as the DCS $\sigma(\theta)_{B1}$. At large angles of $\theta>50°$, the DCS's $\sigma(\theta)_{A1}$ and $\sigma(\theta)_{B1}$ both have a minimum and a maximum. Both $\sigma(\theta)_{A2}$ and $\sigma(\theta)_{B2}$, furthermore, begin to appear around $\theta=45°$ and show almost the same angular dependence. These results at $E_{lab}=1500$ eV suggest that there are two different types of excitation mechanisms, one is the one-electron transitions taking place at larger internuclear distances, and the other is one- and two-electron excitations at smaller distances.

Angular and energy dependences of the DCS $\sigma(\theta)_{B1}\sin\theta$ of one-electron charge transfer in the laboratory system are shown in Fig. 8, where the abscissa is the reduced angle of $\tau=E_{lab}\theta$. The open triangles and solid and open circles are the DCS's measured at $E_{lab}=650$, 1000, and 1500 eV, respectively. The DCS depends strongly on the angle and energy at small angles of $\tau<20$ keV deg, while it does rather weakly at large angles of $\tau>20$ keV deg. The result at $E_{lab}=1000$ eV has a distinct structure at $\tau<15$ keV deg, while such a clear structure cannot be observed in the DCS's at other energies of $E_{lab}=650$ and 1500 eV.

Figure 9 exhibits the DCS $\sigma(\Theta)$ in the c.m. system at large angles of $\Theta>55°$ and c.m. energy of $E=952$ eV ($E_{lab}=1500$ eV) evaluated from the DCS's of the scat-

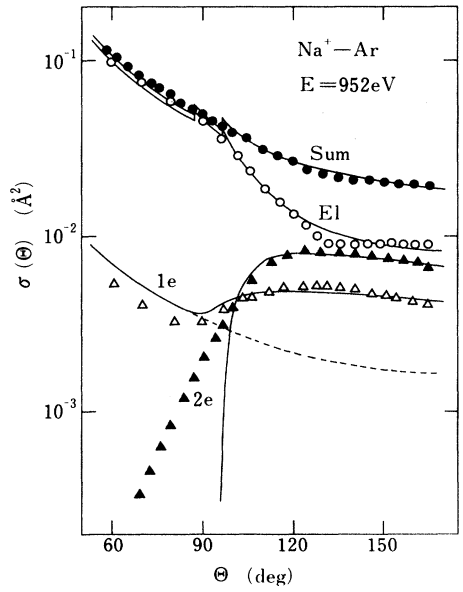

FIG. 9. Angular dependence of the DCS $\sigma(\Theta)$ in the c.m. system for Na^+-Ar at the energy $E=952$ eV ($E_{lab}=1500$ eV). ● and ○, experimental summed and elastic DCS's, respectively. △ and ▲, experimental DCS's of one- and two-electron excitations, respectively. ——, calculated DCS's. — — —, calculated partial DCS of the one-electron transitions.

tered Na^+ ions and Na atoms, and of the recoiled Ar atoms and Ar^+ ions. The open and solid circles are the elastic DCS $\sigma(\Theta)_{el}$ and the summed DCS $\sigma(\Theta)_{sum}$, respectively. Open and solid triangles give the DCS's $\sigma(\Theta)_{1e}$ for one-electron excitations and $\sigma(\Theta)_{2e}$ for two-electron excitations, respectively. Here, $\sigma(\Theta)_{1e}$ and $\sigma(\Theta)_{2e}$ both are the sum of the DCS's for the charge transfer and direct excitation of Ar atoms.

2. Li^+-Ar collisions

Differential scattering measurements for Li^+-Ar collisions have been performed at energies of $70 \leq E_{lab} \leq 350$ eV. The DCS's of the Li^+ ions and Li atoms measured at $E_{lab}=350$ eV are presented in Fig. 10. The solid circles denote the DCS $\sigma(\theta)_{B1}$ of the Li atoms produced by one-electron charge transfer, which was evaluated with the detection efficiency ε for the Li atoms of the multiplier. As seen in the figure, the DCS $\sigma(\theta)_{B1}$ begins to appear around $\theta=10°$ and has a distinctly oscillating structure, which was also observed in the DCS measured at the lower energy $E_{lab}=200$ eV. As mentioned above, the maxima in the DCS $\sigma(\theta)_{B1}$ are predominantly due to the Li atoms produced by reaction (8). The open triangles in Fig. 10 are DCS's $\sigma(\theta)_{A1}$ of direct excitation of Ar atoms by reactions (7). The DCS $\sigma(\theta)_{A1}$ has small values and depends only weakly on the scattering angle. Open circles represent the summed DCS $\sigma(\theta)_{sum}$. In Fig. 10, the

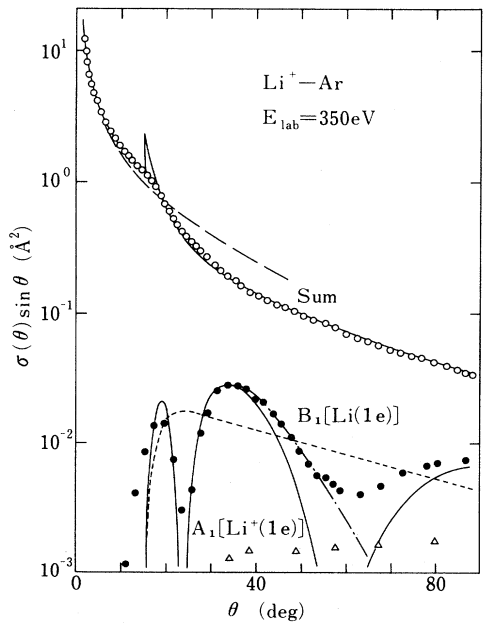

FIG. 10. Angular dependence of the DCS $\sigma(\theta)\sin\theta$ of the scattered Li^+ ions and Li atoms in the laboratory system for Li^+-Ar at $E_{lab}=350$ eV. ● and △, experimental inelastic DCS's $\sigma(\theta)_{B1}$ and $\sigma(\theta)_{A1}$, respectively. ○, experimental summed DCS $\sigma(\theta)_{sum}$. — —, calculated elastic DCS. ——, calculations of the DCS's $\sigma(\theta)_{sum}$ and $\sigma(\theta)_{B1}$. —·—·—, DCS $\sigma(\theta)_{B1}$ calculated with the two-term potentials. — — —, DCS $\sigma(\theta)_{B1}$ calculated without the interference effect.

relative DCS $\sigma(\theta)_{sum}$ measured at the small angles $\theta<10°$ is fitted to the elastic DCS calculated with the experimental potential [18]

$$V(R)=1750\exp(-4.24R)\ \text{eV}\ , \tag{11}$$

which is given by the broken curve. Electronic transition in the low-energy Li^+-Ar collisions is very weak, nevertheless, the calculated DCS is always higher than the experimental summed DCS at angles of $\tau>7$ keV deg ($\theta>20°$ for $E_{lab}=350$ eV). This suggests that the potential function of Eq. (11) must be corrected at smaller distances.

III. ANALYSES OF EXPERIMENTAL RESULTS

A. Ground-state potentials

For quantitative discussions of excitation mechanisms in the collisions, one has to first determine the ground-state potential as accurately as possible. Excited-state potentials and potential parameters at critical distances, where electronic transition takes place, can be evaluated with the analysis of experimental DCS's based on knowledge about the ground-state potential.

1. Na^+-Ar collisions

The ground-state potential in the Na^+-Ar system was directly evaluated from the elastic DCS at $E_{lab}=200$ and 350 eV in Fig. 5 by employing the inversion method developed by Firsov [36]. In the inversion procedure, the deflection function $\Theta(b)$ as a function of impact-parameter b is first deduced from the angular dependence of the DCS. The potential energy $V(R)$ can be uniquely determined from the function $\Theta(b)$. The direct inversion method needs elastic DCS over the full angular range ($0° \leq \Theta \leq 180°$). Since the experimental DCS is available only at $\Theta \geq 3°$, the DCS at small angles of $\Theta<3°$ was evaluated here by using the experimental potential of Eq. (10). The potential of this system has an attractive well so shallow, -0.19 eV [37], that the contribution of the attractive part was neglected. The solid curve in Fig. 11(a) represents the repulsive potential derived with the inversion method at $4<V(R)<200$ eV ($0.65<R<1.7$ Å). The inversion results can be approximately fitted to an analytical form

$$V(R)=9080\exp(-4.49R)-(11.561R)^7\exp(-13.3R)$$
$$-(18.385R)^7\exp(-21.0R)\ \text{eV}\ , \tag{12}$$

within an error of 2%. The solid curves in Fig. 5 are the elastic DCS calculated with Eq. (12). The calculations satisfactorily reproduce the DCS's measured at the lower energies $E_{lab}=70$ and 125 eV, as well as those for $E_{lab}=200$ and 350 eV.

As seen in Fig. 11(a), the ground-state potential does not lie on a straight line in the logarithmic scale, but shows an inclination structure. The solid curve in Fig. 11(b) presents the potential gradient $\alpha(R)=-d\ln V(R)/dR$, deduced directly from the inversion results, which has a minimum value $\alpha_m \simeq 3.0$ Å^{-1} at

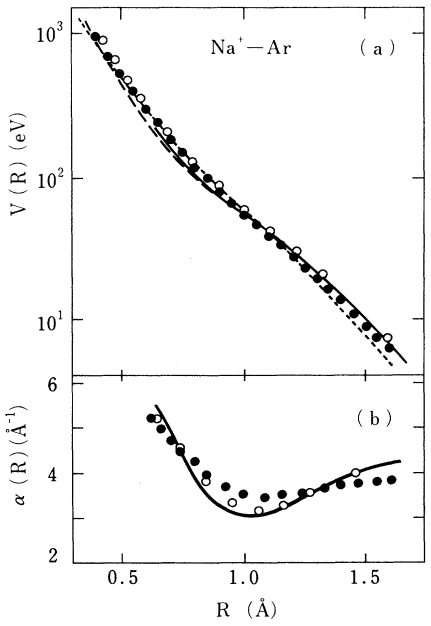

FIG. 11. (a) Ground-state potentials for Na^+-Ar. —— and — —, experimental potentials deduced by the inversion and curve-fitting procedures, respectively. ○ and ●, calculations with the *ab initio* method and the statistical electron-gas model, respectively. — — —, empirical model potential. (b) Potential gradient in the logarithmic scale. ——, experimental result. ○ and ●, *ab initio* and statistical calculations, respectively.

$R \simeq 1.02$ Å.

The inelastic signals observed at $E_{lab}=650$ and 1000 eV are still lower than 10% of the total intensity, which can be seen in Fig. 6. The ground-state potential at shorter distances was also evaluated from the summed DCS's for $E_{lab}=650$ and 1000 eV by the curve fitting of the DCS. The result is given by

$$V(R)=9080\exp(-4.49R)-(11.561R)^7\exp(-13.3R) -(19.468R)^7\exp(-21.0R)\ \text{eV} . \quad (13)$$

The broken curve in Fig. 11(a) denotes this potential. The solid curve in Fig. 7 exhibits the summed DCS calculated with Eq. (13) by assuming elastic scattering. The calculation reproduces well the experimental summed DCS over the whole angular range. The ground-state potential of Eq. (13) is valid at least up to $V(R)\sim 900$ eV ($R\sim 0.4$ Å).

2. Li^+-Ar collisions

The ground-state potential at shorter distances for Li^+-Ar was deduced by the curve fitting of the experimental summed DCS at lower energies of $E_{lab}=125$ and 200 eV, by assuming elastic scattering. The deduced potential is given by

$$V(R)=1750\exp(-4.24R) -(9.741R)^9\exp(-20.0R)\ \text{eV} . \quad (14)$$

The potential of Eq. (14) has an inclination structure around $R_{inc}=0.74$ Å, similar to the case of Na^+-Ar. The DCS calculated with Eq. (14) also reproduces well the experimental summed DCS at $E_{lab}=350$ eV, shown in Fig. 10, over the whole angular range. The potential function is valid at the potential height $V(R)\leq 250$ eV ($R\geq 0.4$ Å).

B. Excited-state potentials

1. Li^+-Ar collisions

In the low-energy Li^+-Ar collisions, electronic transition is predominantly due to the charge-exchange reaction (8). The charge-transfer DCS $\sigma(\theta)_{B1}$ has a distinctly oscillating structure, as shown in Fig 10. The oscillatory structure in the DCS strongly depends on the difference $\Delta V(R)=V_2(R)-V_1(R)$ between ground- and excited-state potentials [15]. One can then evaluate the excited-state potential for reaction (8), as well as the ground-state potential by the fitting of the DCS $\sigma(\theta)_{B1}$. According to Barat *et al.* [11], the electronic transition in this colliding system takes place through the noncrossing interaction rather than the crossing interaction. However, the experimental results suggest that the transition occurs at a localized internuclear distance. In this study, elastic and inelastic DCS's were calculated semiclassically by assuming the Landau-Zener transition probability at the critical (crossing) distance

$$p=\exp(-2\pi V_{12}^2/\hbar\Delta S v_r) , \quad (15)$$

where V_{12} is the interaction energy, ΔS is the difference in slopes of the two potential curves, and v_r is the radial velocity. Diabatic ground- and excited-state potentials were initially estimated by referring the ground-state potential of Eq. (14). In the fitting procedure, the DCS $\sigma(\theta)_{B1}$ was calculated iteratively as a function of the potential parameters and of the interaction energy V_{12} at the critical distance to get a best fit of the DCS $\sigma(\theta)_{B1}$.

The solid curves in Fig. 10 give the calculated optimum results of the summed and charge-exchange DCS's. The computed DCS $\sigma(\theta)_{B1}$ is normalized to the experiments at the second maximum, $\theta\simeq 35°$. The dotted curve in Fig. 10 is the charge-transfer DCS calculated without the interference between two trajectories. Both the calculations reproduce satisfactorily the overall feature of the experiments. The potentials determined by the data analysis are

$$V(R)_1=1750\exp(-4.24R)-(9.581R)^9\exp(-20.0R) +19\,000\exp(-18.0R)\ \text{eV} \quad (16)$$

and

$$V(R)_2=1912\exp(-4.60R)-(9.581R)^9\exp(-20.0R) +17\,000\exp(-19.2R)+10.4\ \text{eV} . \quad (17)$$

The dot-dashed curve in Fig. 10 shows the DCS $\sigma(\theta)_{B1}$ calculated by using Eqs. (16) and (17) without the third terms. This curve reproduces the experiments only at an-

TABLE I. Crossing parameters for Li^+-Ar, deduced from experiments.

R_C (Å)	$V(R_C)$ (eV)	ΔS (eV/Å)	V_{12} (eV)	R_{inc}[a] (Å)	r_i+r_j[b] (Å)
0.81	47.0	27.5	2.68	0.74	0.86

[a]Inclination point in the experimental ground-state potential.
[b]Evaluation from the ionic and atomic radii.

gles of $\theta < 60°$. In order to explain the experimental DCS $\sigma(\theta)_{B1}$ over the whole angular range, we have to assume three-term potentials. The DCS $\sigma(\theta)_{B1}$ measured at $E_{lab}=200$ eV can also be fairly reproduced by the calculations. The potential parameters at the critical (crossing) point, which characterize the electronic transition, are listed in Table I.

2. Na^+-Ar collisions

The electronic transitions in the Na^+-Ar collisions are classified into two types of mechanisms, i.e., one-electron excitation taking place at the angles $\tau < 60$ keV deg, and one- and two-electron excitations occurring at $\tau > 60$ keV deg. These two mechanisms will be discussed here separately. Figure 12 represents a schematic drawing of the diabatic potentials employed in the data analyses. Here, V_1 is the ground-state potential, and V_2 and V_3 are the potentials leading to the singly and doubly excited states, respectively. One-electron transition is assumed here to take place through outer crossing C_1 and inner crossing C_2, and two-electron transition through inner crossing C_3.

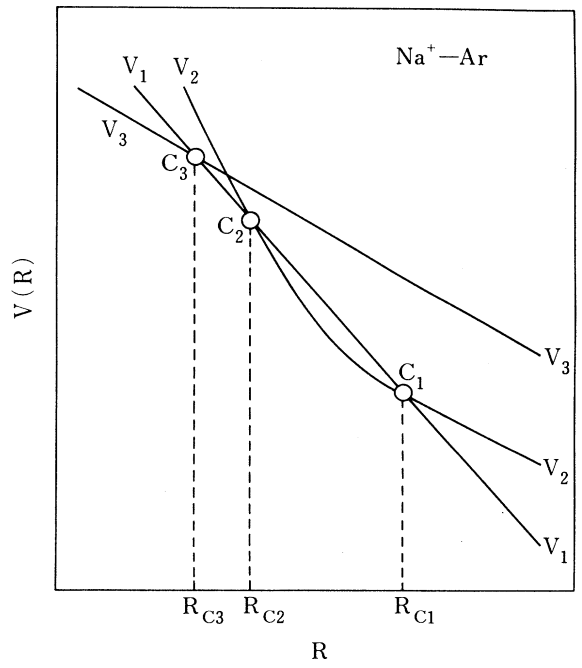

FIG. 12. Schematic drawing of diabatic potentials for Na^+-Ar. V_1, V_2, and V_3 represent the ground-, singly excited-, and doubly excited-state potentials, respectively.

(i) *Excitation through outer crossing.* At lower energies of $E_{lab} \leq 1000$ eV, the electronic transition is predominantly due to the charge-exchange reaction (1). The excited-state potential V_2 for reaction (1), as well as the ground-state potential V_1, were evaluated by curve fitting of the charge-transfer DCS $\sigma(\theta)_{B1}$. Taking into account the overall features of the DCS $\sigma(\theta)_{B1}$ in Figs. 6 and 8, the fitting has been performed for $E_{lab}=650$ and 1000 eV.

The solid curves in Fig. 6 show the fitting results of the charge-transfer DCS and the summed one. The calculated charge-transfer DCS is normalized to the experiments near threshold ($\theta < 15°$). The calculations fairly reproduce the experiments for $E_{lab}=650$ eV. The diabatic ground- and excited-state potentials deduced experimentally are

$$V_1 = 9080\exp(-4.49R) - (11.372R)^7\exp(-13.25R) - (19.468R)^7\exp(-21.0R)\ \text{eV} \quad (18)$$

and

$$V_2 = 11\,240\exp(-4.85R) - (11.391R)^7\exp(-13.30R) - (20.044R)^7\exp(-21.0R) + 10.6\ \text{eV}, \quad (19)$$

respectively. The crossing parameters R_{C1}, V_{12}, ΔS_1, and $V(R_{C1})$ deduced from the experiments are presented in Table II.

The solid curves in Fig. 8 exhibit the angular and ener-

TABLE II. Crossing parameters for Na^+-Ar deduced from the experiments.

Parameter	Value
Crossing radii (Å)	
R_{C1}	1.07
R_{C2}	0.452
R_{C3}	0.440
Threshold energies (eV)	
$V(R_{C1})$	46.2
$V(R_{C2})$	646
$V(R_{C3})$	700
Slopes (eV/Å)	
ΔS_1	24.9
ΔS_2	297
ΔS_3	385
Interactions (eV)	
$V_{12}(C_1)$	3.0
$V_{12}(C_2)$	6.3
$V_{13}(C_3)$	5.2
Radii (Å)	
R_{inc}[a]	1.02
r_i+r_j[b]	0.96
$\lvert r_i-r_j\rvert$[b]	0.38

[a]Inclination point in the experimental ground-state potential.
[b]Evaluations from the ionic and atomic radii.

gy dependences of the charge-transfer DCS $\sigma(\theta)_{B1}$ that are calculated by assuming the potentials of Eqs. (18) and (19) and without the interference effect. The calculations adequately explain the drastic energy dependence observed in the experimental DCS around the threshold angle $\tau=7$ keV deg. For $E_{\rm lab}=650$ and 1000 eV, the calculations also satisfactorily reproduce the experiments at larger angles of $\tau>20$ keV deg. Nevertheless, the calculations for $E_{\rm lab}=1500$ eV are higher than the experiments at $\tau>10$ keV deg. The DCS $\sigma(\theta)_{B1}$ calculated with the two-state approximation reproduces preferably the sum of the experimental inelastic DCS's, $\sigma(\theta)_{1e}=\sigma(\theta)_{A1}+\sigma(\theta)_{B1}$, which is represented by the dotted curve in Fig. 8.

(ii) *Excitation through inner crossing.* At high energy $E_{\rm lab}=1500$ eV, one-electron excitations are due to reactions (1)–(4). Nevertheless, the calculations with the potentials of Eqs. (18) and (19) explain fairly well the experimental summed inelastic DCS $\sigma(\theta)_{1e}$ of one-electron transitions at $E_{\rm lab}=1500$ eV (the dotted curve in Fig. 8). Then, the potential V_2, leading to reaction (1), was also employed to calculate the DCS $\sigma(\Theta)_{1e}$ in Fig. 9. The potential V_2 of Eq. (19) was corrected to better reproduce the experimental $\sigma(\Theta)_{1e}$ at $\Theta>80°$, with the ground-state potential of Eq. (18) being kept the same. Potential V_3, which leads to two-electron excitation, was also deduced by the fitting of the DCS $\sigma(\Theta)_{2e}$ in Fig. 9.

The solid curves in Fig. 9 are the best results of the DCS's calculated without the interference effect. The calculations satisfactorily reproduce the overall feature of the experiments. The disagreement between the calculation and experiment for two-electron excitation at $\Theta<100°$ is due to the neglect of the tunneling effect in the calculation, which is important near threshold. The dotted curve in Fig. 9 represents the partial DCS $\sigma(\Theta)_{1e}$ (outer) due to only the outer crossing, which was evaluated by neglecting the transition at the inner crossing. The potentials V_2 and V_3, evaluated from the experiments, are given by

$$V_2=11\,240\exp(-4.85R)-(11.391R)^7\exp(-13.30R)$$
$$-(20.084R)^7\exp(-21.0R)+10.6\ \text{eV} \quad (20)$$

and

$$V_3=8830\exp(-4.35R)-(11.392R)^7\exp(-13.30R)$$
$$-(20.044R)^7\exp(-21.0R)+29\ \text{eV}\ . \quad (21)$$

The crossing parameters deduced from the experiments are listed in Table II.

IV. COMPUTATION OF REPULSIVE POTENTIALS

The ground-state potential determined experimentally shows a specific inclination structure, as discussed above. The inclination point $R_{\rm inc}=1.02$ Å for Na^+-Ar is nearly equal to the outer-crossing radius $R_{C1}=1.07$ Å determined experimentally. This is almost the same for the Li^+-Ar system. The charge-transfer DCS measured at lower energies for Li^+-Ar shows a typical oscillatory structure, while the inelastic DCS for Na^+-Ar has only a weakly undulating structure. In order to elucidate these specific features, *ab initio* potentials of ground and lowest-excited states have been calculated with a multiconfiguration self-consistent field (MCSCF) method. The computations were carried out by using the quantum-chemistry code GAMESS revised by Schmidt *et al.* [38]. The active space of the MCSCF calculations includes all valence orbitals and electrons. In the calculations, we have used the McLean-Chandler extended basis set [39] augmented by double sets of six d functions for Li, Na, and Ar atoms. The orbital exponents of the polarization functions are 0.1 and 0.4 for the Li atom, 0.0875 and 0.35 for the Na atom, and 0.425 and 1.7 for the Ar atom. Therefore, our basis set has the quality of triple ζ plus double polarizations. The ground-state potential has also been calculated with the statistical electron-gas model, which provides reasonably reliable repulsive potentials for closed-shell particles [40].

The open and solid circles in Fig. 11(a) exhibit the ground-state potentials for Na^+-Ar computed by the MCSCF method and the statistical model, respectively. Both the calculations agree fairly well with the experiments. The open and solid circles in Fig. 11(b) denote the gradient α evaluated from the MCSCF potentials and the statistical calculations, respectively. The *ab initio* calculations give a minimum value $\alpha_m\simeq3.15$ Å^{-1} around $R_{\rm inc}=1.05$ Å, which is similar to the experiment, while the statistical calculations provide a somewhat shallow minimum $\alpha_m\simeq3.45$ Å^{-1} at $R_{\rm inc}\simeq1.05$ Å. The difference in the gradient α between the two calculations may be due to interactions between the ground and excited states, because the statistical model does not involve the interactions. The inclination point in the experimental and theoretical potentials, $R_{\rm inc}=1.02$–1.05 Å, is nearly equal to the crossing radius $R_{C1}=1.07$ Å determined experimentally, and also to the sum of the ionic and atomic radii defined by the outermost atomic orbital $r_i+r_j=0.96$ Å [41].

The ground-state potentials calculated with the MCSCF method and the statistical model for Li^+-Ar also agree well with the experimental result of Eq. (14) at $R>0.4$ Å, and have the inclination structure around $R_{\rm inc}=0.77$ and 0.85 Å, respectively. The inclination points coincide adequately with the experimental distances $R_{\rm inc}=0.74$ Å and $R_C=0.81$ Å given in Table I, and also with the sum of ionic and atomic radii $r_i+r_j=0.86$ Å. Thus, the inclination point $R_{\rm inc}$ in the ground-state potentials for the asymmetric Na^+-Ar and Li^+-Ar systems has a close relation to the distances R_C and r_i+r_j.

The overall feature of the ground-state potential can be understood by the empirical overlap model for the repulsive potential [20]. The model potential for the interacting partners i and j is given by the overlap of the electron clouds ρ_i and ρ_j,

$$V(R)=C_{ij}\int\rho_i(\mathbf{r}_a)\rho_j(\mathbf{r}_b)d\mathbf{r}\ , \quad (22)$$

where r_a and r_b are the distances from the nuclei a and b to a point in the overlap region, respectively, and

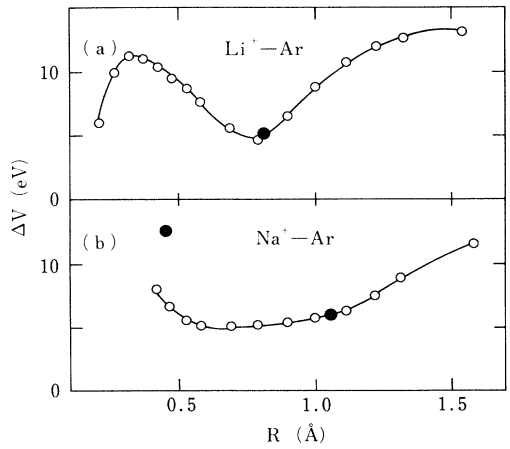

FIG. 13. Difference potentials $\Delta V = V_2 - V_1$ for (a) Li^+-Ar and (b) Na^+-Ar. ○ and ●, *ab initio* calculations and experiments, respectively.

$\mathbf{r}_a - \mathbf{R} = \mathbf{r}_b$. The proportionality factor C_{ij} is determined by the relation of $dV/dR = -0.72$ eV/Å at a specific distance R_{ij} [21(a)], which is the sum of the atomic radii defined by the electron-density distribution in the outer region of each atom [21(c)]. The dotted curve in Fig. 11(a) shows the model potential for Na^+-Ar calculated with the electron density that was evaluated from the analytical wave functions [41]. The empirical model potential agrees with the experimental and theoretical potentials within 30% over the whole range in the figure. This is almost the same for Li^+-Ar.

The open circles in Fig. 13 exhibit the difference potential $\Delta V = V_2 - V_1$ for the Li^+-Ar and Na^+-Ar systems obtained by the *ab initio* calculations. The result for Li^+-Ar is nearly equal to that of Barat *et al.* [11]. The solid circles in the figure give the energy separations of the adiabatic potential at the critical distance $\Delta V(R_C) = 2V_{12}$, evaluated from the experimental interaction energy $V_{12}(R_C)$. As shown in the figure, the experimental energy separations $\Delta V(R_C)$ for Li^+-Ar and $\Delta V(R_{C1})$ at the outer crossing for Na^+-Ar coincide well with the calculations. However, the experimental $\Delta V(R_{C2}) = 12.6$ eV for Na^+-Ar is much higher than the theoretical $\Delta V \simeq 7.5$ eV at R $(= R_{C2}) = 0.45$ Å. For Li^+-Ar, the calculated difference $\Delta V(R)$ has a narrow minimum around $R = 0.8$ Å, which is nearly equal to the experimental crossing radius $R_C = 0.81$ Å. However, the theoretical ΔV for the Na^+-Ar has a broad minimum at $0.5 < R < 1.1$ Å. The experimental radius $R_{C1} = 1.07$ Å corresponds to the largest distance for the broad minimum in the theoretical difference potential ΔV.

V. DISCUSSION

The *ab initio* calculations suggest that the broad minimum in the difference potential $\Delta V = V_2 - V_1$ at $0.5 < R < 1.1$ Å for Na^+-Ar is due to the potential approach rather than the avoided crossing, similar to Li^+-Ar. The difference ΔV has a narrow minimum for Li^+-Ar, but a broad minimum for Na^+-Ar. Then, the electronic transition is considered to take place through the noncrossing interactions at a localized distance in the low-energy Li^+-Ar collisions, while it takes place within a somewhat broad range of distances in the Na^+-Ar collisions. This should be the reason for the experimental findings that the charge-transfer DCS $\sigma(\theta)_{B1}$ shows a well-resolved oscillatory structure for Li^+-Ar, but only a weakly undulating structure for Na^+-Ar.

The correlation between the critical distance R_C and the sum of the ionic and atomic radii $r_i + r_j$ (or inclination point R_{inc}) suggests that R_C is related to the maximum in the overlap O_{ij} of radial charge density $P = r^2\rho(r)$ of the outermost atomic orbital. The calculated overlap O_{ij} for Na^+-Ar has double maxima, which appear around the distances $R \simeq r_i + r_j$ and $|r_i - r_j|$. The distance $|r_i - r_j| = 0.38$ Å for Na^+-Ar coincides fairly well with the inner-crossing radii $R_{C2} = 0.45$ Å and $R_{C3} = 0.44$ Å determined experimentally.

One- and two-electron excitations through the inner crossing for Na^+-Ar can be understood by the molecular-orbital (MO) correlation diagram [16]. In this system, the $4d\sigma$ MO correlating with the atomic-orbital Ar $3p$ is promoted to cross the $4p\sigma$ and $4s\sigma$ MO's, which correlate with Na $3s$ and Ar $4s$, respectively. The one- and two-electron excitations at shorter distances are attributed to the MO crossings. The feature of the MO crossing for the asymmetric Na^+-Ar system resembles that of the quasisymmetric K^+-Ar system, in which the $5f\sigma$ MO correlating with Ar $3p$ is promoted to cross the MO's correlating with K $4s$ and Ar $4s$. However, the excitational features are completely different for these two systems. As discussed above, the inner-crossing distance $R_{C2} = 0.45$ Å for Na^+-Ar is close to the difference between the atomic radii, $|r_i - r_j| \simeq 0.38$ Å. However, the potential crossing for K^+-Ar appears at the distance $R_C \simeq 1.2$ Å [8], which is close to the sum of the atomic radii $r_i + r_j = 1.3$ Å. In the K^+-Ar collisions the DCS of one-electron charge transfer, which produces K($4s$) atoms, is especially large near threshold (transition probability $P \sim 1$), while the DCS $\sigma(\Theta)_{1e}$ of one-electron transitions for Na^+-Ar due to the inner crossing is smaller than that for two-electron excitations, as can be seen in Fig. 9.

The outer-crossing distance $R_{C1} = 1.07$ Å for the one-electron transition in the Na^+-Ar collisions is in good agreement with the crossing radius $R_C = 1.06$ Å for the Na($3s \rightarrow 3p$) transition in the Na-Ar system [28]. The electronic transition in Na-Ar has been discussed by relating it with the direct excitation of Ar atoms, which corresponds to reaction (2) in the Na^+-Ar collisions. At the angle $\tau = 15$ keV deg for $E_{\text{lab}} = 1500$ eV, the Na($3s \leftarrow 3p$) emission probability in the Na-Ar collisions is approximately 30% of the summed DCS [28], which is about 50 times larger than the excitation probability $P = \sigma(\theta)_{A1}/\sigma(\theta)_{\text{sum}} \simeq 0.006$ for reactions (2) and (3) in the Na^+-Ar collisions shown in Fig. 7. Around the crossing radius $R_C = 1.06$ Å, the ground-state potential V_1 for Na-Ar and the excited-state potential V_2' for Na-Ar($4s$) are considered to be nearly equal to those for

Na^+-Ar and Na^+-Ar($4s$), respectively, because the outermost electron Na($3s$) with the large radius $r_i = 1.8$ Å contributes only weakly to the potential. The energy separation $\Delta V = V_2' - V_1$ at the critical distance for Na^+-Ar, which will be nearly equal to that for Na-Ar, was roughly estimated from the experimental DCS $\sigma(\theta)_{A1}$ to be 7 eV. The separation $\Delta V = 7$ eV is much larger than the excitation energy for the Na($3s \rightarrow 3p$) transition, $Q = 2.1$ eV. The electronic transition in Na-Ar, therefore, will be due to direct interaction between the ground- and lowest excited-state potentials, which is related to the inclination structure in the repulsive potentials, the same as for charge-exchange reactions in the Na^+-Ar system. This will also be true for the K($4s \rightarrow 4p$) transition in the K-Hg collisions [29].

VI. SUMMARY

Electronic transitions in the Na^+-Ar collisions were observed at laboratory energies of $E_{lab} > 500$ eV. For energies of $500 < E_{lab} < 1000$ eV, the transition probability is so small that the inelastic signals could scarcely be detected. The dominant inelastic signal at the lower energies is due to the charge-exchange reaction of the one-electron transition. The DCS of direct excitation of the Ar atoms is less than 30% of that for the charge-exchange reaction. However, two-electron excitation with a larger transition probability was observed at energies of $E_{lab} > 1000$ eV. The electronic transitions for Na^+-Ar are classified into two types of excitation mechanisms. One is the one-electron transitions with smaller probability at larger distances. The other is the one- and two-electron transitions with larger probability at smaller distances.

Diabatic ground- and excited-state potentials for Na^+-Ar were deduced from the experimental DCS's by assuming potential crossings of three states. The analyses of the experimental DCS's indicate that the one-electron transitions with small probability take place at distances of $R < R_{C1} = 1.07$ Å, and one- and two-electron transitions with larger probability occur at $R < R_{C2} = 0.45$ Å. The former transition is due to the approach of ground- and excited-state potentials, while the latter is attributed to the crossings of the promoted $4d\sigma$ MO, which correlates with the atomic-orbital Ar $3p$. The critical radii $R_{C1} = 1.07$ Å and $R_{C2} = 0.45$ Å are close to the distances $r_i + r_j = 0.96$ Å and $|r_i - r_j| = 0.38$ Å, respectively, evaluated from ionic and atomic radii.

ACKNOWLEDGMENTS

We are very grateful for a long-standing dialogue with the late Professor Emeritus H. Inouye (Tohoku University, Sendai, Japan). We also gratefully acknowledge Professor M. Izawa (National Laboratory High Energy Physics, Tsukuba, Japan) for his contributions to this work. This work was financially supported in part by the Matsuo Foundation and by Grants-in-Aid for Scientific Research from the Ministry of Education, Science and Culture of Japan.

[1] D. C. Lorents and G. M. Conklin, J. Phys. B **5**, 950 (1972).
[2] R. Francois, D. Dhuicq, and M. Barat, J. Phys. **5**, 963 (1972).
[3] J. C. Brenot, D. Dhuicq, J. P. Gauyacq, J. Pommier, V. Sidis, M. Barat, and E. Pollack, Phys. Rev. A **11**, 1245 (1975).
[4] V. V. Afrosimov, Yu. S. Gordeev, and V. M. Lavrov, Zh. Eksp. Teor. Fiz. **68**, 1715 (1975) [Sov. Phys. JETP **41**, 860 (1976)].
[5] J. P. Gauyacq, J. Phys. B **9**, 2289 (1976); **11**, 85 (1978).
[6] V. Sidis, N. Stolterfoht, and M. Barat, J. Phys. B **10**, 2815 (1977).
[7] J. Ø. Olsen, T. Andersen, M. Barat, Ch. Courbin-Gaussorgues, V. Sidis, J. Pommier, J. Agusti, N. Andersen, and A. Russek, Phys. Rev. A **19**, 1457 (1979).
[8] S. Kita, M. Izawa, and H. Inouye, J. Phys. B **16**, L499 (1983); S. Kita, M. Izawa, T. Hasegawa, and H. Inouye, *ibid.* **17**, L885 (1984); S. Kita, H. Tanuma, and M. Izawa, *ibid.* **20**, 3089 (1987).
[9] J. C. Mouzon, Phys. Rev. **41**, 605 (1932).
[10] V. V. Afrosimov, Yu. S. Gordeev, V. M. Lavrov, and V. K. Nikulin, in *Abstracts of Papers, Proceedings of the Seventh International Conference on the Physics of Electronic and Atomic Collisions, Amsterdam, 1971,* edited by L. M. Branscomb *et al.* (North-Holland, Amsterdam, 1971), p. 143.
[11] M. Barat, D. Dhuicq, R. Francois, and V. Sidis, J. Phys. B **6**, 2072 (1973).
[12] K. Niurao and H. Inouye, J. Phys. Soc. Jpn. **40**, 813 (1976).
[13] B. I. Kikiani, M. R. Gochitashvili, R. V. Kvizhinadze, and V. A. Ankudinov, Zh. Eksp. Teor. Fiz. **87**, 1906 (1984) [Sov. Phys. JETP **60**, 1096 (1984)].
[14] J. C. Brenot, D. Dhuicq, J. P. Gauyacq, J. Pommier, V. Sidis, M. Barat, and E. Pollack, Phys. Rev. A **11**, 1933 (1975).
[15] R. E. Olson and F. T. Smith, Phys. Rev. A **3**, 1607 (1971).
[16] U. Fano and W. Lichten, Phys. Rev. Lett. **14**, 627 (1965); M. Barat and W. Lichten, Phys. Rev. A **6**, 211 (1972).
[17] J. E. Jordan and I. Amdur, J. Chem. Phys. **46**, 165 (1967); I. Amdur, J. E. Jordan, K. R. Chien, L. W. M. Fung, R. L. Hance, E. Hulpke, and S. E. Johnson, *ibid.* **57**, 2117 (1972); I. Amdur, M. J. Engler, and J. E. Jordan, *ibid.* **63**, 597 (1975).
[18] H. Inouye and S. Kita, J. Phys. Soc. Jpn. **34**, 1588 (1973).
[19] S. Kita, K. Noda, and H. Inouye, J. Chem. Phys. **63**, 4930 (1975).
[20] S. Kita, K. Noda, and H. Inouye, J. Chem. Phys. **64**, 3446 (1976).
[21] (a) T. L. Gilbert, J. Chem. Phys. **49**, 2640 (1968); (b) F. T. Smith, Phys. Rev. A **5**, 1708 (1972); (c) E. H. Carlson, J. Chem. Phys. **58**, 1905 (1973).
[22] Y. S. Kim, S. K. Kim, and W. D. Lee, Chem. Phys. Lett. **80**, 574 (1981).
[23] N. Esbjerg and J. K. Nørskov, Phys. Rev. Lett. **45**, 807 (1980); R. B. Laughlin, Phys. Rev. B **25**, 2222 (1982).
[24] P. Bisgaard, T. Andersen, B. V. Sørensen, S. E. Nielsen, and J. S. Dahler, J. Phys. B **13**, 4441 (1980).

[25] K. H. Blattmann, M. Dold, W. Schäuble, L. Zehnle, and V. Kempter, J. Phys. B **13**, 3389 (1980).
[26] S. Kita, H. Tanuma, I. Kusunoki, and Y. Sato, Phys. Rev. A **42**, 367 (1990).
[27] K. Jørgensen, N. Andersen, and J. Ø. Olsen, J. Phys. B **11**, 3951 (1978).
[28] N. Andersen, T. Andersen, K. Bahr, C. L. Cocke, E. H. Pedersen, and J. Ø. Olsen, J. Phys. B **12**, 2529 (1979).
[29] R. Düren, H. Hübner, S. Kita, and U. Krause, J. Chem. Phys. **85**, 2751 (1986).
[30] H. Inouye, M. Izawa, S. Kita, K. Takahashi, and Y. Yamato, Bull. Res. Inst. Sci. Meas. Tohoku Univ. **32**, 41 (1984).
[31] S. Kita, S. Furusawa, H. Tanuma, I. Kusunoki, and M. Ishigame, Bull. Res. Inst. Sci. Meas. Tohoku Univ. **37**, 33 (1988).
[32] M. Izawa, S. Kita, and H. Inouye, J. Appl. Phys. **53**, 4688 (1982).
[33] S. Kita and H. Inouye, J. Mass Spectrom. Soc. Jpn. **41**, 211 (1993).
[34] F. A. Morse and R. B. Bernstein, J. Chem. Phys. **37**, 2019 (1962).
[35] S. Kita, K. Noda, and H. Inouye (unpublished).
[36] O. B. Firsov, Zh. Eksp. Teor. Fiz. **24**, 279 (1953); G. H. Lane and E. Everhart, Phys. Rev. **120**, 2064 (1960); U. Buck, Rev. Mod. Phys. **46**, 369 (1974).
[37] L. A. Viehland, Chem. Phys. **85**, 291 (1984).
[38] M. W. Schmidt, K. K. Baldridge, J. A. Boatz, J. H. Jensen, S. Koseki, M. S. Gordon, K. A. Nguyen, T. L. Windus, and S. T. Elbert, Quantum Chem. Prog. Exch. Bull. **10**, 52 (1991).
[39] A. D. McLean and G. S. Chandler, J. Chem. Phys. **72**, 5639 (1980).
[40] Y. S. Kim and R. G. Gordon, J. Chem. Phys. **60**, 4323 (1974); V. K. Nikulin and Yu. N. Tsarev, Chem. Phys. **10**, 433 (1975).
[41] E. Clementi, IBM J. Res. Dev. Suppl. **9**, 2 (1965).